Materials and Design 166 (2019) 107611

Contents lists available at ScienceDirect

Materials and Design

journal homepage: www.elsevier.com/locate/matdes

Study on microstructure and tensile properties of high nitrogen Cr-Mn steel processed by CMT wire and arc additive manufacturing

Xiaoyong Zhang [a,b], Qi Zhou [a,*], Kehong Wang [a], Yong Peng [a], Jialuo Ding [b], Jian Kong [a], Stewart Williams [b]

[a] School of Materials Science and Engineering, Nanjing University of Science and Technology, Nanjing 210094, China
[b] Welding Engineering and Laser Processing Center, Cranfield University, Cranfield MK43 0AL, UK

HIGHLIGHTS

- High nitrogen austenite stainless steel parts were successfully made by CMT-WAAM process with excellent tension properties.
- The increased density of inclusions (0.1-1μm) surrounding by Cr2N was detrimental to tension properties after heat treatment.
- Migration of δ-γ boundaries during high-temperature short-time heat treatment reveals a great promotion of the YS and UTS.
- YS and UTS anisotropies were largely reduced due to the stable austenite matrix and nitrogen work hardening effect.

GRAPHICAL ABSTRACT

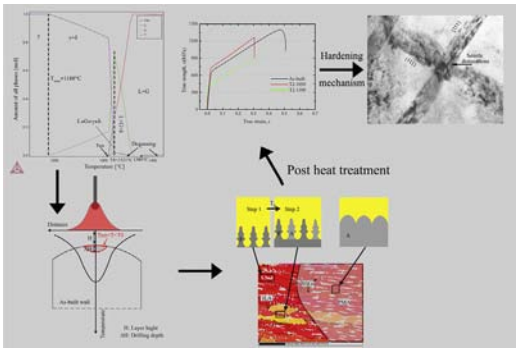

ARTICLE INFO

Article history:
Received 24 November 2018
Received in revised form 9 January 2019
Accepted 18 January 2019
Available online 23 January 2019

Keywords:
High nitrogen Cr-Mn steel
CMT wire and arc additive manufacturing (CMT-WAAM)
Post heat treatment
Solidification model
Inclusions
Nitrogen work hardening

ABSTRACT

A designed Cr-Mn-N wire with 0.99 wt% of nitrogen content (HNS0.99) was used to make high nitrogen austenite stainless steel parts by introducing CMT wire and arc additive manufacturing (CMT-WAAM) method. The solidification behaviour, microstructure evolution, inclusions and tension properties were studied both in the as-built and post heat treatment conditions. Excellent tension properties parts with high nitrogen content were successfully produced. Ferrite-austenite (FA) and austenite-ferrite (AF) solidification models were revealed in the as-built microstructure of two different areas, inner layer area (ILA) and partial melting area (PMA), respectively, and the former predominated the microstructure. Amorphous inclusion islands and microspherical inclusions made by MnO were found. The increasing density of the latter in 0.1-1 μm diameters was detrimental to the tensile properties because the matrix-inclusion surfaces acted as the preferred nucleation sites for Cr_2N during heat treatment. Due to the stable austenite and the nitrogen work hardening effect, planer dislocation-arrays predominated the dislocation slip model which, to some extent, diminished the strength anisotropy in different directions. However, the ferrite dendrites caused the diversity of UTS and elongation by acting as tunnels for cracks in the horizontal direction samples.

© 2019 The Authors. Published by Elsevier Ltd. This is an open access article under the CC BY-NC-ND license (http://creativecommons.org/licenses/by-nc-nd/4.0/).

1. Introduction

During the last several decades, researchers payed close attention to high nitrogen steels (HNSs) all over the world owing to their fantastic combination of high yield strength, toughness, corrosion resistance, low cost and human body friendliness [1–6]. Solid solution nitrogen in

* Corresponding author.
E-mail address: cheezhou@njust.edu.cn (Q. Zhou).

https://doi.org/10.1016/j.matdes.2019.107611
0264-1275/© 2019 The Authors. Published by Elsevier Ltd. This is an open access article under the CC BY-NC-ND license (http://creativecommons.org/licenses/by-nc-nd/4.0/).

alloy matrixes plays a crucial role in these remarkable properties. For higher solubility of nitrogen, high chromium and high manganese levels were added to the alloys. The classic examples for the application of high nitrogen Cr-Mn stainless steels are the austenitic retaining ting materials P900 and P2000 [7]. Specific casting combining with forging such as cold rolling, hot rolling and thermomechanical methods provide the central processing ways for producing these kinds of materials [8–12]. Although high-performance parts were successfully produced, there are also some limitations such as massive equipment cost, long time consumption and environmental pollution.

The advantages of wire and arc additive manufacturing (WAAM) process are widely recognized by researchers and include such benefits as low cost, full deposition density, excellent properties and high efficiency [13,14]. Cold metal transfer (CMT) melting technology does well on the heat input control and steady transfer model [15], so, in this study, it prevails as the heat source during the WAAM process. Cong [16] and Gu [17,18] applied the CMT-WAAM process to the building of aluminium alloy components and found that Al parts can be successfully made by this method and the porosity problem can be adjusted by carefully choosing the CMT model or adding interpass cold rolling process. Mehnen and Ding [19] did extensive work on the shape and manufacturing strategy on the CMT-WAAM fabrication process, and many active surface finishing parts were built. After mechanical tests, Xu [20] found that the WAAM made steel parts presented a positive performance in strength and elongation when compared with the wrought sheet. Similar results were reported by Posch [21] when contrasted to the all-weld metal parts. However, in Chen's report [22] the mechanical properties were lower than the wrought pieces due to the existence of sigma phase in the 316 L stainless steel CMT-WAAM made parts. So, the CMT-WAAM process was a promising and low-cost way for manufacturing alloy parts under carefully processed control.

Until now, there are few reports about the combination of High nitrogen Cr-Mn steel and CMT-WAAM technology. Some reasons can be concluded, such as the difficulty in making suitable wire, unknown welding ability and the porosity problem. These obstacles were also found in the welding process of HNSs [23–25]. In the past several decades, researchers focused on improving nitrogen content in the weld bead and keeping them in the solid solution state other than in the form of nitride or pore. Some practical ways of achieving this were discovered such as improving the nitrogen partial pressure during welding [26–29] and adding some surface active elements like oxygen [30] or surplus [31]. As reported by Stein [7] Cr, Mn could dramatically increase the nitrogen solubility during smelting and an underlying problem is the fact that any elements enhancing nitrogen content will also improve the tendency of nitride formation, such as Cr, Ti, Nb and V. Besides nitrides, the solidification model of HNSs revealed a noticeable effect on the porosity formation [32]. Proper solidification behaviour will be carefully controlled from the chemical component design to the careful selection of processing methods [29,33,34]. So, it is necessary to explore the performance both of microstructure and mechanical properties of HNS by using CMT-WAAM technology to explore the potential advantages of this kind of material and the method.

In this paper, we developed a high nitrogen Cr-Mn wire with 0.99 wt % nitrogen (HNS0.99), and it was used to build HNS parts. The solidification behaviour, phase and inclusion morphologies along with their evolution during post heat treatments have been studied as well as the correlated mechanical properties.

2. Experimental procedure

2.1. Material preparation and CMT-WAAM process

The HNS steel wire (HNS0.99) used in this study was made through melting, casting, rolling, drawing, and air cooling. The annealing process was added to the procedure if there was necessary with the temperature of 1000 °C. The nitrogen content was adjusted by using nitriding ferroalloys to the melt [35]. The chemical composition of the HNS wire is represented in Table 1. The dimension of the base metal is $300 * 150 * 10$ (mm).

The CMT-WAAM system in the present study mainly consisted of a six-axle Yaskawa robot, a set of CMT heat source and two-axle working platform. A commercial ternary gas-mixer was used in this research with ±2.5% accuracy and wide gas-mixing rang (0–5% for oxygen/0–100% for nitrogen/0–100% for argon). Pure oxygen, nitrogen and argon were used to produce the shielding gas with the 99.99% purity. Fig. 1a shown the sketch of deposition. Depositing parameters are listed in Table 2 with the reference during welding HNSs such as improving the nitrogen partial pressure above the molten pool to prevent the formation of nitrogen pores [36] and enhancing molten pool surface activity elements to improve the nitrogen absorption [37]. Arc running speed (ARS) was fixed as 30 cm/min, and the total flow rate of shielding was 30 L/min with the stable wire feed speed (WFS) of 6 m/min. A laser high-speed pyrometer M322 of Sensor Therm with the detecting range from 800 to 3000 °C was used to measure the molten pool surface temperature during a single CMT welding process with the same parameters used in the CMT-WAAM process, as shown in Fig. 1b. The emissivity was chosen 0.33, and the collecting interval was set as 1 msec per data.

2.2. Phase and inclusion evolution

Two single-pass multi-layer walls (As-built and T2) with 250 mm length and 150 mm height were deposited with the interface temperature below 100 °C. T2 was dived vertically into two parts from the middle of the wall, one of them (T2-1050) was heated to 1050 °C, held on 5 min and then water quenched. The other (condition T2-1100) was heated to 1100 °C, kept on 30 min and then water quenched. Samples were spark cut from the as-built wall, T2-1050 and T2-1100 for metallographic analysis and EBSD examination. Extracting positions and dimensions of the specimens are shown in Fig. 1c. Metallographic samples were ground, polished for 5-8 min and electrically etched. The electrolyte was a 40 wt% NaOH solution. Each sample was etched with 3 V DC for 30 s until the sample surface became straw yellow. The microstructure was firstly observed by an optical microscope (OM, Optiphot Nikon). Then, they were analyzed with the Scanning Electron Microscope (SEM, FEI XL30-SFEG) and the TESCAN Lyra3 dual beam SEM system equipped with the energy-dispersive spectrometry detector (EDS) for high magnification observation and elements detection. Lastly, the samples were gradually ground and polished for 40 min and then photos were taken for the quantitative analysis of the inclusions. After that, they were used for phase contents and secondary phases precipitation by using an INCA Crystal EBSD system, Oxford Instruments. The phase identification was carried out by using X-ray diffraction (SIEMENS D5005) with Cu Kα radiation ($\lambda = 1.5418$ Å).

2.3. Tensile and microhardness testing

Tensile samples were cut by the spark from the three walls (as-built, T2-1050 and T2-1100) in the vertical direction (VD) parallels to the deposition direction and horizontal direction (HD) parallels to the arc running direction. At least three samples were taken in each direction. The tension samples were painted with the graphite and then equipped with the reflective tape to measure the elongation during the tensile test (gauge length = 35 mm) through the laser extensometer. The dimension and positions of the tension samples were shown in Fig. 1c. Experiments were conducted at Instron 5500R electromechanical testing machine (load cell: 50 kN, crosshead speed: 1 mm/min) at room temperature. Thin films were taken by the TESCAN Lyra3 dual beam SEM system near the fracture area in the tension samples and the T2-1100 metallographic sample for transmission electron microscopy (TEM, Philips CM10) studies at 200 kV with the EDS system. The

Table 1
Chemical composition of homemade HNS wire (HNS0.99).

	C	Mn	Cr	Mo	Ni	N	Si	P	S	Cu	Co	Fe
HNS0.99	0.028	17.86	22.7	1.19	2.08	0.99	0.18	0.015	0.01	0.008	0.022	Residual

microhardness was measured using a Zwick/Roell hardness tester under a load of 300 g and holding time of 15 s.

3. Results

3.1. Microstructure characterization and evolution

Fig. 2 shows the microstructure of the wall under the as-built condition (T1) on the YZ face (a) and XY face (b) along with their high magnifications (c) and (d), respectively. From Fig. 2(a,c), it can be seen that dendrite δ-ferrite and columnar austenite (γ) with some inclusion islands predominated the microstructure. Both δ-ferrite and γ revealed a preferred crystallographic direction which was the cubic-on-cubic direction (⟨100⟩ directions for BCC and FCC) and extended across numerous build layers, as frequently found by researchers [20–22] during the WAAM process. Visible inclusion islands distributed randomly in the as-built matrix. There are two distinct areas in a single layer, the inner-layer area (ILA) and partial melting area (PMA). In the ILA, δ-ferrite revealed two morphologies, the skeletal shape and the lathy pattern, besides the former took the central part (Fig. 2(a,c)). In the PMA (Fig. 2 (b,c,d)), the secondary arms of both skeletal ferrite and lathy ferrite were partially melted. After analysis by the quantitative metallography method, the average space between the adjacent δ-ferrite dendrites was around 33.3 μm in ILA and 11.9 μm in PMA. This shrunken space means, except the remaining ferrite, some new ferrite dendrites were generated after the subsequent solidification and caused the increase of ferrite dendrites in this area. The new ferrite dendrites and the relevant solidification model will be discussed later.

Fig. 3 gives the microstructure under condition T2-1050 (a) and T2-1100 (c) along with their detailed views (b) and (d), respectively. From Fig. 2a, δ-ferrite can be discriminated from γ, and most of the ferrite dendrites were broken, besides some secondary arms have disappeared. Secondary austenite (γ_2) was found in front of δ-dendrites along with the uniform needle or film-like precipitations (about 1.7 μm in length), as shown in Fig. 3b. It can be assumed that the precipitation phases are chromium nitrides (CrN or Cr_2N) considering the texture and the formation position, according to the reports by [38–40]. After treatment by condition T2-1100, it is difficult to distinguish ferrite dendrite from austenite as the further transformation which made the disappearance of secondary arms and the discontinuous of ferrite dendrites, as shown in Fig. 3c. Besides, some rod-like precipitations propagating around the inclusion island were observed under high magnification, as shown in Fig. 3d. The mechanism of the formation of these precipitations will be discussed later.

3.2. Tension properties

Table 3 gives the mechanical performance (yield strength (YS), ultimate strength (UTS) and elongation) of the as-built, T2-1050 and T2-1100 tension samples. The as-built parts revealed an outstanding performance of YS, UTS and elongation with the values, >550 Mpa, >850 Mpa and >30%, respectively. For T2-1050 samples, both YS and UTS got a distinct improvement by 104.4–105.6 Mpa for YS and 31.6–80.6 Mpa for UTS. However, a decrease of elongation, with the values around 12%, happened. When the as-built parts were heat treated to 1100 °C for 30 min, the overall behaviour of the parts dropped significantly with the values of 86.3–133.2 Mpa for YS, 54.8–86.3 Mpa for UTS and 0.6–27.3% for elongation.

Fig. 4 shows the SEM maps of tension samples in the VD under the as-built (a,b), T2-1050 (c,d) and T2-1100 (e,f) conditions with their magnified pictures. The as-built tension samples revealed a strong ductile fracture tendency with large amounts of dimples and voids with spherical inclusions in them. Two distinction areas were revealed in Fig. 4b, considering that more ferrite dendrites remained in the PMA which caused the reduction of ductility, the area with large shallow voids or dimples was located in the PMA, and the tiny deep dimples were in the ILA. This means a weakened area was formed due to the propagation of PMA. After the EDS detection, the main content of the spherical inclusions remained in the centre of dimples or voids was Mn and O, as shown in Fig. 4b. Mn oxides were presumed to be the primary form of these inclusions considering the shielding gas containing 0.8% oxygen. Mixed fracture patterns were found with quasi-cleavage facets and ductile dimples in the T2-1050 condition. The dimples were larger and shallower than that of the as-built condition. Spherical inclusions still existed in the shallow voids, however, with a lower content than that in the as-built condition. Tiny, but shallow, voids with massive inclusion island caused cavities were shown in the T2-1100 condition. The spherical inclusions, like that in the T2-1050 sample, kept to a lower level.

Fig. 5 is the SEM fracture surface maps of the HD tension samples with their magnified pictures under the as-built (a,b), T2-1050 (c,d)

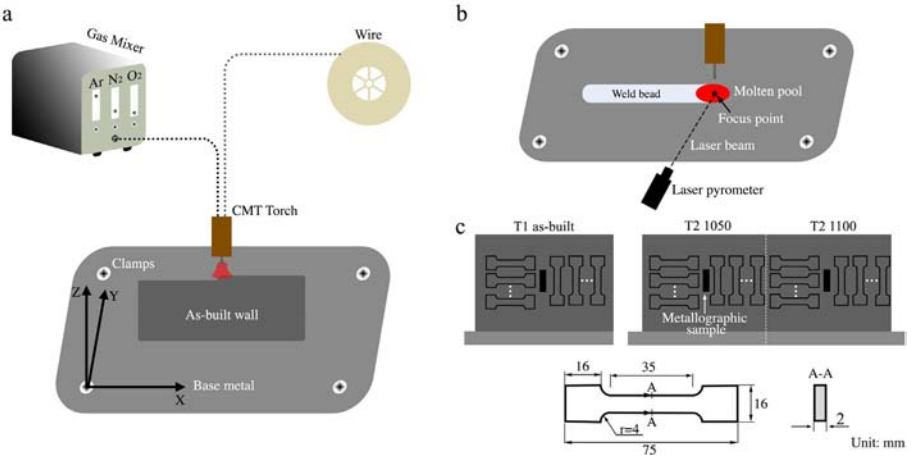

Fig. 1. (a) Layout of the deposition process (b) Sketch of molten pool surface temperature measurement, (c) spark cutting positions of tension/metallographic samples along with the dimensions.

Table 2
CMT-WAAM process parameters.

Notation	Unite	Level
WFS	m/min	6.0
CMT model		CMT + P
O2	L/min	0.24
N2	L/min	1.2
Ar	L/min	28.56
ARS	cm/min	30
Interface T.	°C	<100

and T2-1100 (e,f) conditions. All the samples revealed a strong tendency of ductile fracture. Different from the VD samples, the fracture surface exposed a typical lamellar tearing along the ferrite dendrites which were found in the as-built and T2-1050 conditions. However, the lamellar morphology was a little fuzzy in the T2-1100 condition, as shown in Fig. 5e, due to the longer holding time, causing the further decomposition of ferrite dendrites. In Fig. 5a, the fracture surface of the PMA was found, as revealed in Fig. 4a, with broader and shallower voids. Similar to the condition in VD samples, the PMA also revealed a weak effect in the HD samples when compared to the ILA. The spherical inclusions were still Mn oxides following the results of EDS, as shown in Fig. 5b, and mainly existed in the as-built condition. The fracture models of the T2-1050 and T2-1100 HD samples were the same as the corresponding VD samples. The difference was that, in the HD samples, the cracks mainly propagated along the ferrite dendrites. However, in the VD samples, the fracture surface primarily spread in the austenite matrix with no preferential directions. The inclusion island induced cavities have a higher content in the T2-1100 HD sample which revealed a detrimental effect to the tension properties.

4. Discussion

4.1. Solidification behavior of the inner-layer area (ILA) and partial melting area (PMA)

Thermo-calc software was used to calculate the equilibrium solidification diagram of HNS0.99, and the result was shown in Fig. 6a. It can be seen that the ferrite-austenite (FA) solidification model was revealed. δ-Ferrite was firstly generated in liquid and reached the highest content (red triangle A in Fig. 6a), then ferrite transformation began, simultaneously. The γ phase started to generate from the liquid phase which made the component entered a four-phase coexisted area, as shown by the stripe pattern area in Fig. 6a. At the end of liquid phase area, γ predominated the microstructure with some δ. However, according to the reversed Schaeffler diagram [32], shown in Fig. 6b, the austenite solidification model (A) was calculated with the values of Creq (24.75) and Nieq (19.36), as the red triangle B indicates. The reason for this conflict is the ignorance of the degassing of nitrogen when using the Schaeffler diagram. According to the high-speed laser pyrometer, the molten pool temperature was around 1600 °C during the CMT-WAAM process, as shown in Fig. 7. Which made the degassing process unavoidable as the degassing happened when the temperature is beyond 1380 °C. As a result, solidification model switched from A (L ≥ A) to FA (L ≥ F + A) owing to the lack of austenite stabiliser (N) in the ILA before the red triangle point A. After point A, austenite and ferrite separate from liquid together which lead the component to a four-phase coexist stage as mentioned above. In the ILA, the solidification behaviour initiated from FA with co-separating of austenite and ferrite at the end. According to Fig. 2, the texture in the ILA exactly corresponds to the equilibrium microstructure. So, it can be speculated that the solidification model during the CMT-WAAM process is near to the equilibrium status.

From Fig. 2, there were two kinds of ferrite dendrites which existed in the ILA; plenty of skeletal ferrite with some lathy ferrite. The formation bases are explained as follows. The solidification model switched to FA as the degassing process, and nitrogen received a high concentration in front of primary ferrite dendrites owing to the low solubility of nitrogen in δ-ferrite, as reported by [41]. Consequently, the degassing rate was increasing as shown in stage 1 in Fig. 6a. The diffusion rate kept at a high level due to the segregation of nitrogen along with the high temperature in this period. As a result, austenite started to consume the ferrite at a high rate until there was no sufficient austenite stabiliser or the temperature dropped too low to maintain the high diffusion rate. Finally, skeletal ferrite generated and enriched in ferrite-promoting elements (Cr and Mo) and lack of austenite stabilisers

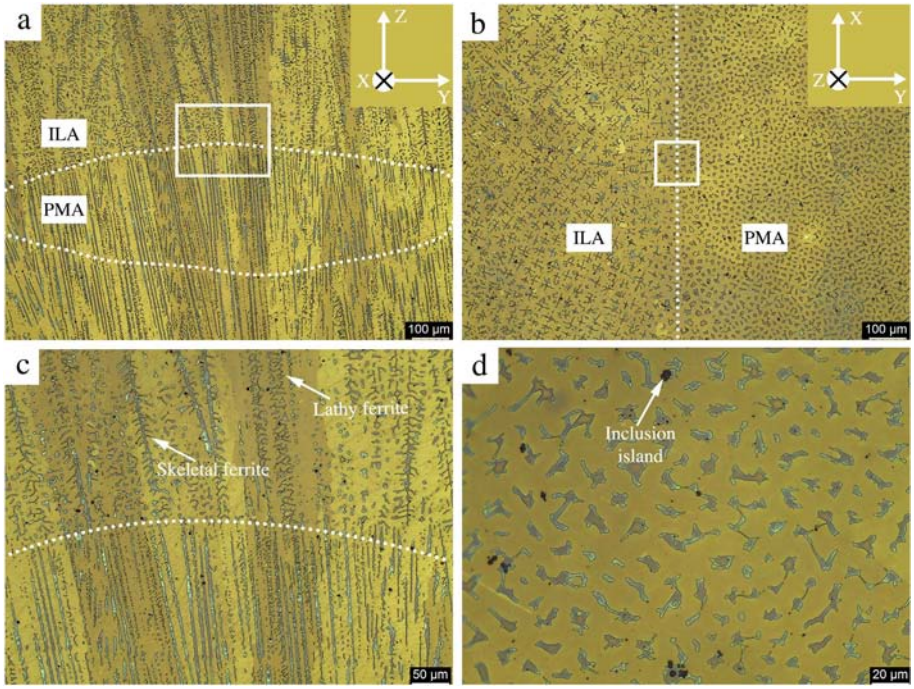

Fig. 2. (a) and (b) describes the microstructure of the as-built wall observed from the YZ face and XY face, (c) and (d) represents the magnified zones in the white rectangles in a and b.

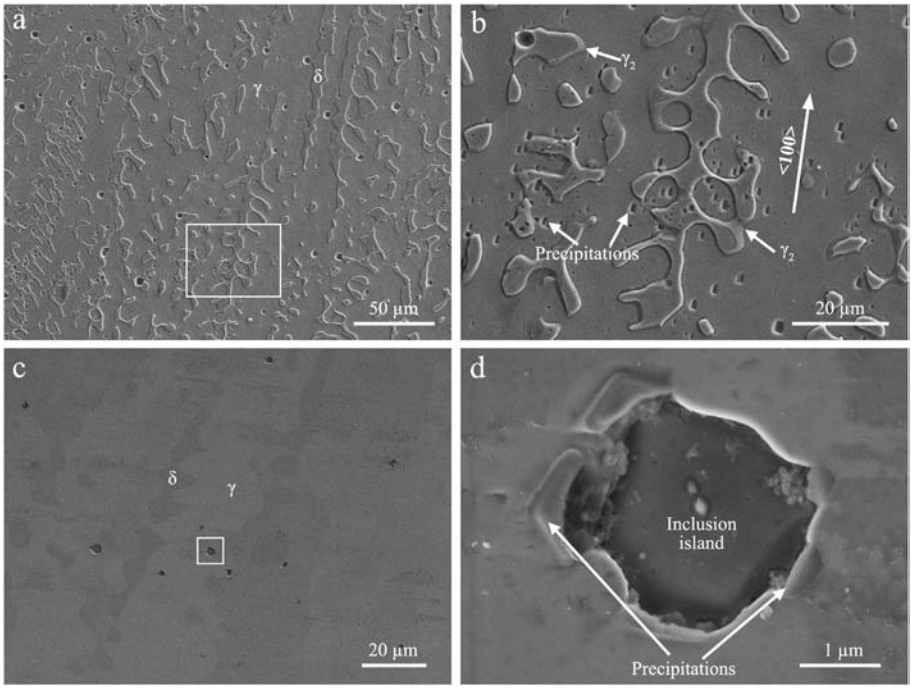

Fig. 3. (a) and (c) shows the microstructure of T2-1050 and T2-1100, respectively. (b) and (d) represents the magnified zones in the white rectangles in a and c.

(N and Ni), as shown in Fig. 8(d,g). However, because of the degassing process, there was no sufficient nitrogen to form austenite fully. As a result, nitrogen concentration in the molten pool kept dropping as the solidification process went on. Besides, with the temperature further dropping, the element diffusion distance reduced gradually. These two reasons restricted diffusion during the ferrite-austenite transformation which made more tightly spaced laths. As a consequence, the residual ferrite pattern cut across the primary dendrite which formed the lathy morphology. So, lathy ferrite is more unstable than skeletal ferrite due to higher austenite promotion elements such as Ni and N and lower ferrite stabilisers (Cr), as shown in Fig. 8(e,h).

The sketch of the PMA generation during the CMT-WAAM process is shown in Fig. 6(c). According to the arc energy distribution bases [42], a similar Gaussian temperature distribution curve existed in the wall along the width direction, as shown by the coordinate system of distance and temperature in Fig. 6c. A higher temperature was expected in the middle of the wall which made a possibility for the extra drilling depth ($\triangle H$) in the centre of the wall reaching T_{sm}. Moreover, considering the phase component in PMA from Figs. 2 and 6d, some residue δ-ferrite dendrites with limited secondary arms existed in the columnar austenite. This means during the subsequent additive process, not all of the metal in this area was melted. So, liquid, austenite and ferrite ($L + \gamma + \delta$) were co-existed simultaneously in this area which corresponded to the stripe pattern area shown in Fig. 6a. As a consequent, the temperature of the PMA (T_{PMA}) addressed between T_{sm} and T_{δ} was acceptable. According to Fig. 8(g,h), the values of Creq/Nieq of austenite adjacent to skeletal ferrite and lathy ferrite were estimated as 1.16 and 1.50, respectively. So, during the re-melting process, the remaining ferrite number was estimated by the grey line, as shown in the Schaeffler diagram. Besides, according to Hammer's report [43], Creq/Nieq < 1.37 reveals the A solidification mode and 1.38 < Creq/Nieq < 1.5 shows the AF solidification model. As a result, solidification in this area would start with austenite. As the degassing process in the first solidification process, nitrogen was not enough to form austenite fully when considering partial melting of δ-ferrite. So, part of liquid would propagate to the grain boundary ferrite phase (GBF) along the solidification subgrain boundaries (SSGs) which caused the tighter space between the ferrite dendrites in this area mentioned in 3.3.1. In this condition, the GBF should be free of nitrogen and enriched in ferrite promoters such as (Cr and Mo) which was proved by the EDS analysis in Fig. 8(f,i). So, the solidification model in this area was confirmed as AF ($L \geq L + A + F \geq A + F$).

In summary, in the ILA, solidification was started with ferrite dendrites and then, at the early stage of ferrite transformation to austenite, some austenite dendrites began to germinate, the solidification model sketch was shown in Fig. 6d. The solidification model in the ILA revealed to be the FA model with co-separating of austenite and ferrite at the end. In the PMA, the columnar austenite generated firstly, as shown in Fig. 6d, with some GBF appeared at the same time. So, the AF model was revealed in the PMA.

4.2. Microstructure evolution during heat treatment

The parts made by the HNS0.99 wire should be a full austenite matrix and free of ferrite or chromium nitrides during the high-temperature heat treatment in T2-1050 and T2-1100 conditions

Table 3
Values of yield strength (YS), ultimate strength (UTS) and Elongation in different conditions of different samples.

Sample	Condition	Position	YS (Mpa)	UTS (Mpa)	Elongation (%)
T1	As-built	HD	575.4 ± 9.61	860.6 ± 8.32	34.9 ± 1.63
		VD	569.5 ± 12.48	851 ± 31.04	46.8 ± 7.2
T2-1050	HT 1050 °C for 5 min	HD	675.1 ± 2.15	892.2 ± 7.8	28.6 ± 2.5
		VD	679.8 ± 12.9	931.6 ± 1.7	39.5 ± 3.7
T2-1100	HT 1100 °C for 30 min	HD	442.2 ± 55.1	663.5 ± 63.59	16.5 ± 4.7
		VD	483.2 ± 49.51	796.2 ± 81.84	34.3 ± 1.4

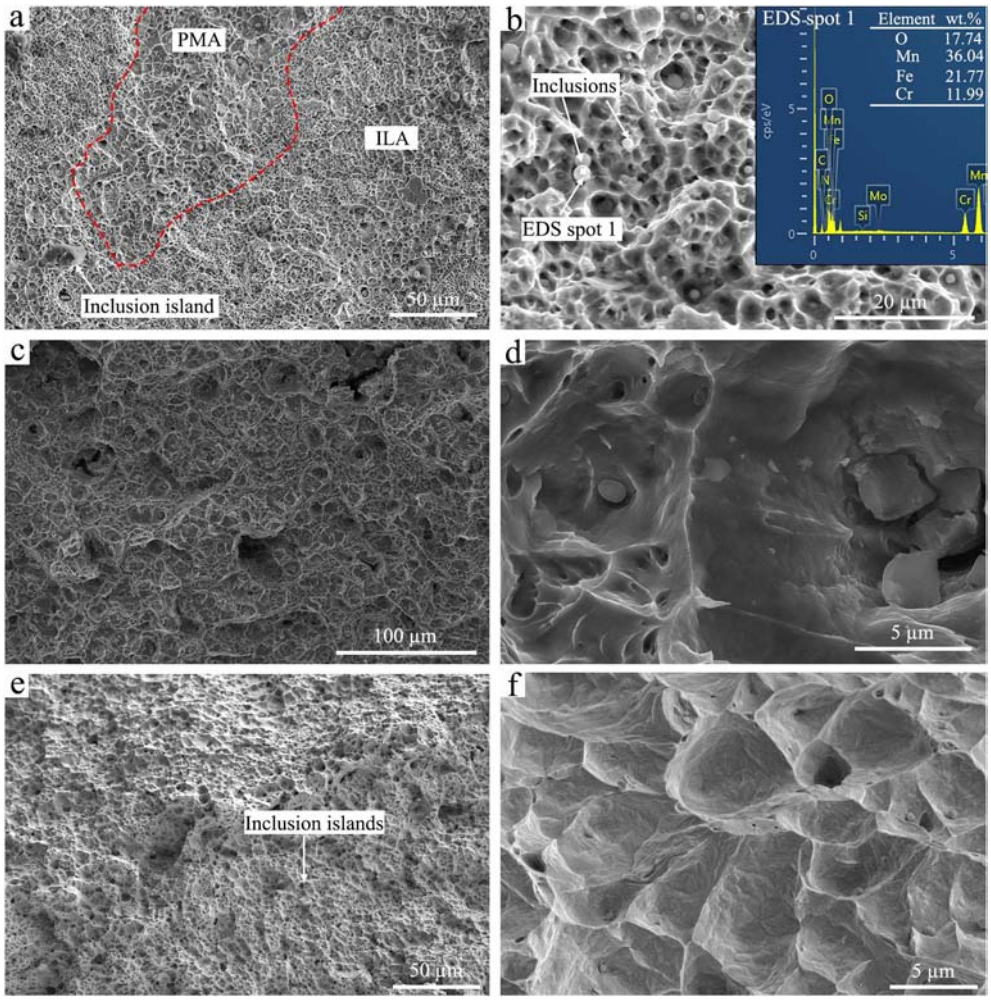

Fig. 4. Tensile fracture surfaces of VD samples: (a,b) as-built, (c,d) T2-1050, and (e,f) T2-1100 conditions.

according to the equilibrium solidification phase diagram represented by the black dot line in Fig. 9a. However, according to the XRD results, there were mainly two phases in the three conditions; austenite and ferrite, besides, some short peaks of Cr_2N and MnO were found in the T2-1100 condition but with very low intensities, as shown in Fig. 9b. This deviation can be explained as follows. As analyzed above, due to the degassing of nitrogen which changed the solidification model from A to FA, as a result, the δ-ferrite was generated. From Fig. 3, during heat treatment, ferrite dendrites were broken gradually with higher heat treatment temperature and a longer holding time, however, always kept existing. There are some reasons for this. Firstly, decomposition of δ-ferrite continuously proceeded during heat treatment due to it being supersaturated with nitrogen. According to Moreno's report [44], nitrogen solubility in ferrite was 0.07 wt%, much lower than 0.21 wt% and 0.57 wt% in skeletal ferrite and lathy ferrite in the as-built condition, as shown in Fig. 8(d,e). The extensive nitrogen content over the solubility limit in δ-ferrite induced the decomposition reaction $\delta \geq Cr_2N/CrN + \gamma_2$, also found in HAZs when welding duplex stainless steels [39]. Secondly, with the continuous consumption of δ-ferrite, the remaining ferrite would be sufficiently enriched in ferrite-promoting elements, Cr and Mo, and, the austenite would contain more austenite-promoting elements, Ni and N, as shown in Fig. 10(c,d,e,f), which caused the residual ferrite more and more stable. As a result, the content of ferrite dendrites kept dropping but had not disappeared.

Fig. 11 shows the variations of nitrogen contents in the γ matrix and the corresponding microhardness in different conditions (a), the EBSD analysis reveals the CrN existed in the T2-1050 sample, and the SEM maps show the Cr_2N precipitated around the inclusion island. According to Fig. 11a, the corresponding equilibrium phase diagrams of the T2-1050 and T2-1100 samples were shown by the red triangle and the blue triangle in Fig. 9a, respectively. In the equilibrium condition, all the nitrogen should be dissolved in the austenite matrix as the solid solution status, and there would be no chromium nitrides. However, in this study, both solid solution nitrogen and chromium nitrides were co-existed. The former was confirmed by the positive correlated effect between microhardness and the nitrogen content in the austenite matrix, as showing in Fig. 11a. This means the nitrogen work hardening effect exists in these three conditions which is a result of solid solution nitrogen in austenite. The latter was revealed by the EBSD analysis (Fig. 11b) and the high resolution of SEM (Fig. 11c). The formation of these chromium nitrides was explained as follows. Due to the continuous decomposition of ferrite and the non-uniform distribution of nitrogen in the matrix, as shown by the error bars in Fig. 11a, chromium nitrides could be generated in some high nitrogen concentration areas or the high energy surfaces between the matrix and inclusions [45], although in the high-temperature heat treatment conditions. Also identified by many researchers, chromium nitrides (Cr_2N or CrN) have been found during the heat treatment process of HNSs. Cr_2N precipitation was mostly found after isothermal ageing of high nitrogen Cr-Mn austenitic steels with the evolution of morphology from intergranular Cr_2N to cellular or lamellar Cr_2N during 700 to 1000 °C [46–49]. CrN always existed in the HAZs during welding high nitrogen steels [39,50] or cooling in the air after ageing [51]. This means CrN preferred to precipitate during the non-equilibrium process and at the nitrogen

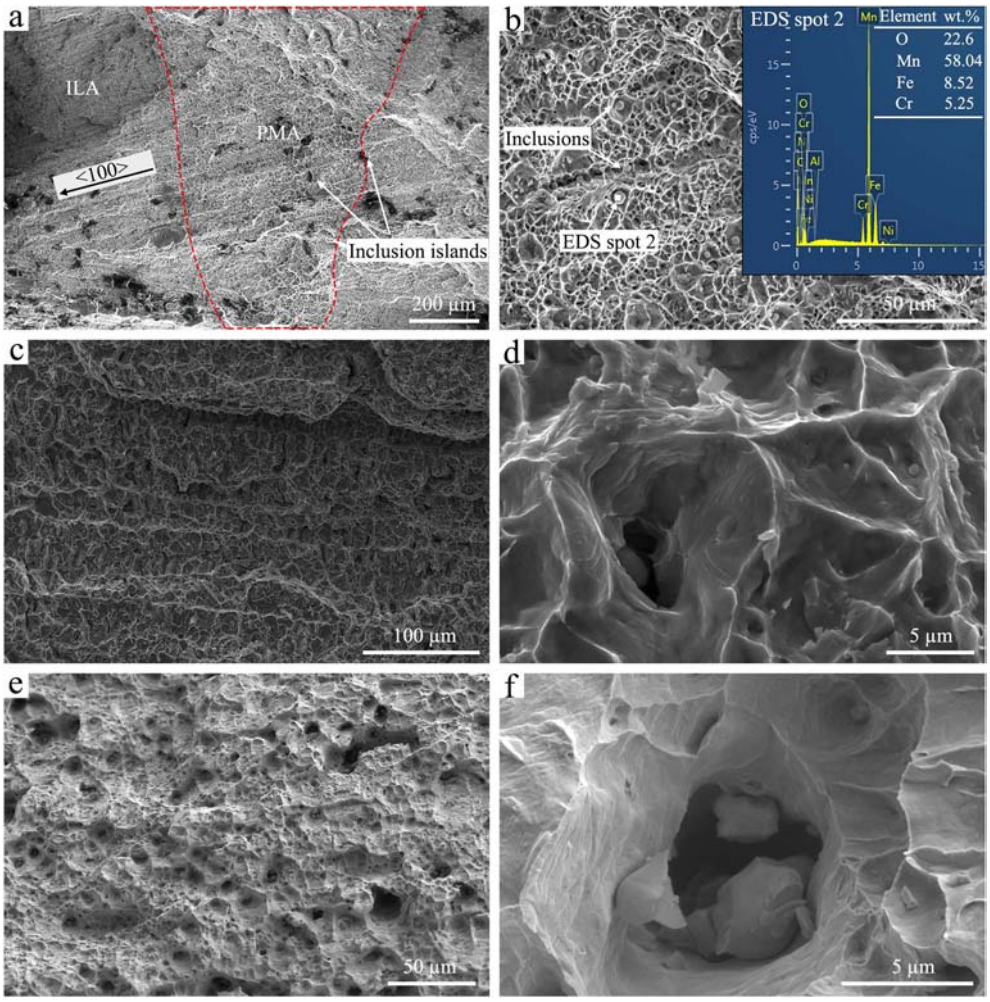

Fig. 5. Tensile fracture surfaces of HD samples: (a,b) as-built, (c,d) T2-1050, and (e,f) T2-1100 conditions.

supersaturated regions. According to Figs. 3b and 11b, plenty of CrN existed in the ferrite dendrites and the inter-dendritic regions with a strong ⟨100⟩ cubic-on-cubic direction. As reported by Kokawa {Kokawa, 1995 #1008} [52], when welding duplex stainless steels, Cr_2N precipitation in ferrite also revealed a ⟨100⟩ texture. A rational conjecture was that CrN firstly generated in the supersaturated nitrogen area, such as in front of the δ-ferrite dendrites, and then grew along the highest thermal gradient. After that, with the growth of ferrite dendrites, some of them were enclosed in the dendrites. During condition T2-1050, the decomposition of δ-ferrite kept generating CrN, and there was not enough time for the existing CrN decomposing into austenite. As a result, a certain amount of CrN scattered in the austenite matrix and the residual ferrite dendrite with the weight percent of 0.12% according to the EBSD analysis. From Figs. 3(c,d) and Fig. 11c, rod-like precipitations were mostly found around the inclusion islands. In Kokawa's [52] report, rod-like Cr_2N was found and nucleated around the oxide inclusions in the weld metal. The reason can be explained that there exist relatively high energy surfaces between the matrix and inclusions. The inclusions act as the inert nucleation surfaces leading to a reduction of the activation energy. Therefore, this kind of inclusions with high energy surfaces can accelerate nucleation of Cr_2N precipitations even at high temperature [45,53,54]. After EDS analysis (as shown in Fig. 12), the inclusion island was mainly formed by Mn oxides. So, it can be presumed that oxide-matrix boundaries acted as preferential nucleation sites for Cr_2N in this case, also proved by the XRD results although with very low-intensity peaks, as shown in Fig. 9b. Further confirmation of Cr_2N and Mn oxides will be shown as follows.

4.3. Effect of size, density and composition of inclusions

Carefully as-polished samples were observed from the OM, and the inclusion distribution maps (at least three areas were selected for each sample) were achieved by using image J software. Due to the remaining micropores having the similar morphology with the inclusions, they were quantitatively analyzed together. Fig. 13 shows the inclusion distribution images and the corresponding histograms of the size and density of the inclusions in different conditions. As shown, the spatial distribution of the inclusions is not uniform (Fig. 13(a,c,e)), and most of the inclusions have diameters in the range of 0.1–1.0 μm (Fig. 13b). Moreover, the T2-1100 sample has the highest area fraction of inclusions (0.67%) among the three, and the others have the rather uniform fractions (0.56% for the as-built sample and 0.55% for the T2-1050 sample). Detailed size and amount distribution of inclusions with the diameters range from 0.1 to 1.0 μm shows that most inclusions in this range distribute between 0.5 and 0.7 μm (Fig. 13(d)). The inclusion densities in the T2-1100 sample reveal relatively higher values when compared with the other two conditions. Since the same deposition conditions in these three samples, the original inclusion content and size distribution should be similar. The reason for this increase can be explained by the generation of Cr_2N around the inclusions <0.1 μm in diameters (which can hardly be seen in OM conditions) in T2-1100 samples. The TEM result combining with the EDS analysis confirmed this kind of precipitation, as shown in Fig. 13c. This, thereby, enlarged these inclusions. This enlargement appearance has more distinct size impact on the inclusions with smaller diameters because the width of the precipitations

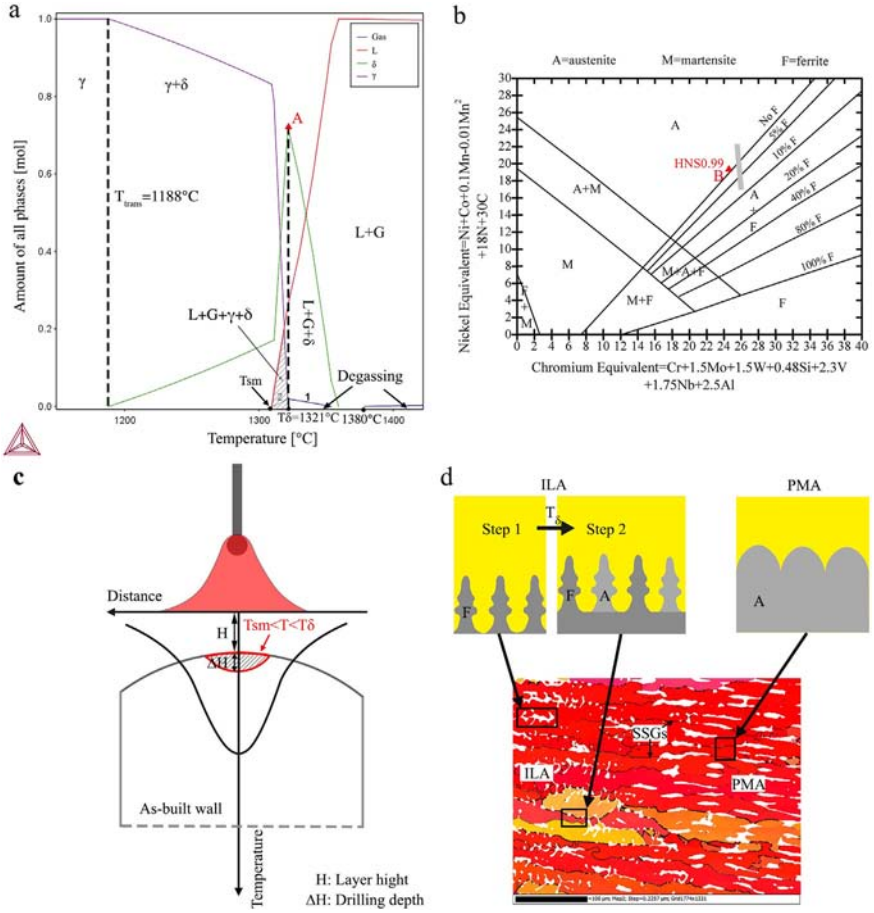

Fig. 6. (a) The solidification property diagram of HNS0.99 calculated with Thermo-calc software, (b) the reversed Schaeffler diagram for the prediction of ferrite number during non-equilibrium solidification process [32], (c) gives the simplified sketch of the PMA formation during CMT-WAAM, (d) the proper solidification models and corresponding EBSD phase diagram in which austenite was colorful with the content of 86.1% and ferrite was white with 12.2% content.

is between 0.03 and 0.4 μm according to Figs. 3d, 11c and 13f. This is the reason why the inclusions with diameters 0.1–1 μm reveal the highest density in T2-1100 condition, and the densities of the inclusions higher than 1 μm in diameter keep almost the same. As a result, the inclusion area fraction in T2-1100 should be the largest among these three conditions, which is provided by the experiment results. According to the previous report [45], the sample with the higher inclusion area fraction revealed the lower toughness. This corresponds to the tensile properties in this study, as shown in Table 3. The tensile properties of T2-1100 samples are poor than the samples of as-built and T2-1050 conditions. It also suggests that the tension properties of the as-built samples should be similar to the T2-1050 samples, which contradicts the results of the experiment. As in Table 3, the tension performance of the T2-1050 samples is more outstanding than the as-built condition samples. This contradiction will be explained later.

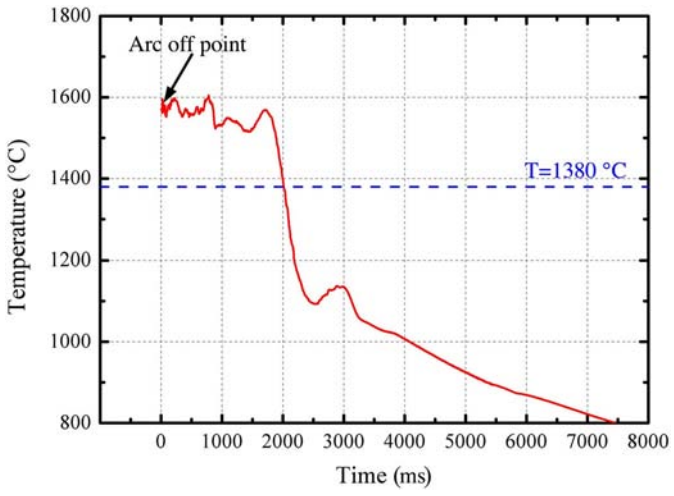

Fig. 7. Molten pool surface temperature distribution after the CMT arc blowout in a single weld bead.

Fig. 14 shows the SEM image of the as-built sample and the element component of the inclusion in the inter-dendritic region. From the EDS analysis, the inclusion is predominated by Mn and O. Due to the oxygen in the shielding gas, a perfect reacting condition was provided for the Mn oxides. So, massive inclusions composed of Mn oxides were generated. Some of them were wrapped up by the matrix, and most of them were concentrated in the front of the solid-liquid interface and pushed by the liquid phase during solidification, as a resulted, these inclusions were focused in the boundaries between austenite and ferrite, as shown in the enlarged region in Fig. 14. According to [37,55,56], in the high nitrogen Cr-Mn metal, MnO is a regular form of Mn-rich oxides which is also confirmed by the XRD results (Fig. 9b) and the TEM analysis (Fig. 13f). This kind of MnO spherical inclusions is also found in the fracture surfaces of different conditions, as shown in Figs. 4, 5. These spherical inclusions always locate in the centre of voids. It can be presumed that MnO particles participated in the fracture process and acted as void nucleation sites. More MnO particles provided more voids which were detrimental to the tension properties owing to the reduction of the active load area. This gives the in-depth explanation of why the T2-1100 samples reveal distressed tension properties, and it corresponds to the discussion above.

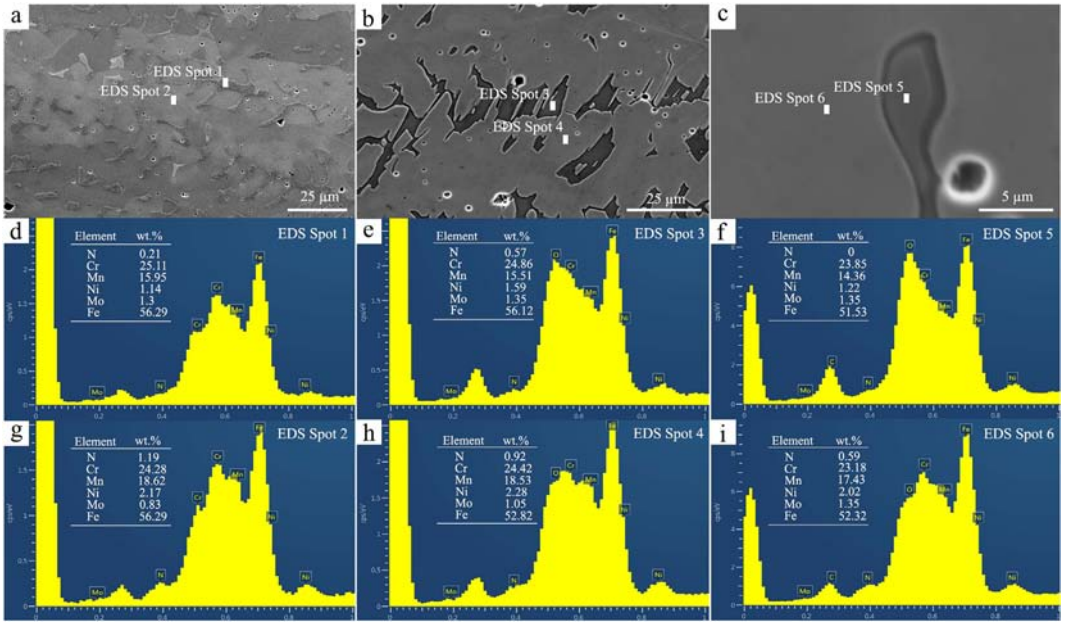

Fig. 8. SEM maps: (a) skeletal ferrite, (b) lathy ferrite and (c) grain boundary ferrite, (d–i) EDS maps: to distinguish element variants in changeable spots; corresponding to the EDS Spots 1–6 in a to c.

4.4. Tensile properties

According to Table 3, samples from the condition T2-1050 revealed prominent advantages in the YS and UTS than the as-built and T2-1100 condition specimens both in HD and VD. Higher values than the as-built samples can be explained by the migration of δ-γ boundary during heat treatment. As shown in Fig. 14a, MnO inclusions segregated at the grain boundary of δ-γ in the as-built condition. As a result, a weak combination of δ – MnO particles – γ was formed. Due to the decomposition of δ-ferrite in condition T2-1050, γ_2 was generated in front of δ-ferrite and continuously transformed to γ phase, as shown in Fig. 3b. A brief sketch of the migration of the δ-γ grain boundaries was shown in Fig. 15. In this case, a stronger joint was formed as δ-γ_2 or γ. As a result, the values of strength were greatly improved, so, heat treatment condition of T2-1050 revealed a positive effect to the tension strength. An opposite effect was shown by long-time heat treatment (T2-1100) samples as relatively low values of the YS and UTS. The formation of Cr_2N precipitation around the inclusions was the primary responsibility as discussed above. Also found by researchers [10,46,50,57], the formation of Cr_2N was detrimental to both strength and elongation. The difference in this study is that the Cr_2N precipitation enlarged the inclusions and increased the area fraction of inclusions which made a smaller active load area during tension tests. As a result, lower tension properties were found. Different to the strength behaviours, the elongation properties were severely reduced both in HD and VD after heat treatment. The generation of chromium nitrides during post heat treatment took the main responsibility.

Anisotropy of tensile ductility did exist in the tension samples due to the preferential growth direction ⟨100⟩ during deposition, as shown in Figs. 2a, 3b and 6d, both columnar austenite and dendritic ferrite revealed a distinct directionality. In HD, crack preferred to generate along the dendrite-austenite boundaries as they were weakened by MnO particles and inclusion islands, at last, the lamellar tearing morphology was formed, as shown in Fig. 5(a,c,e). This was also confirmed by the cross-section of the HD tension sample

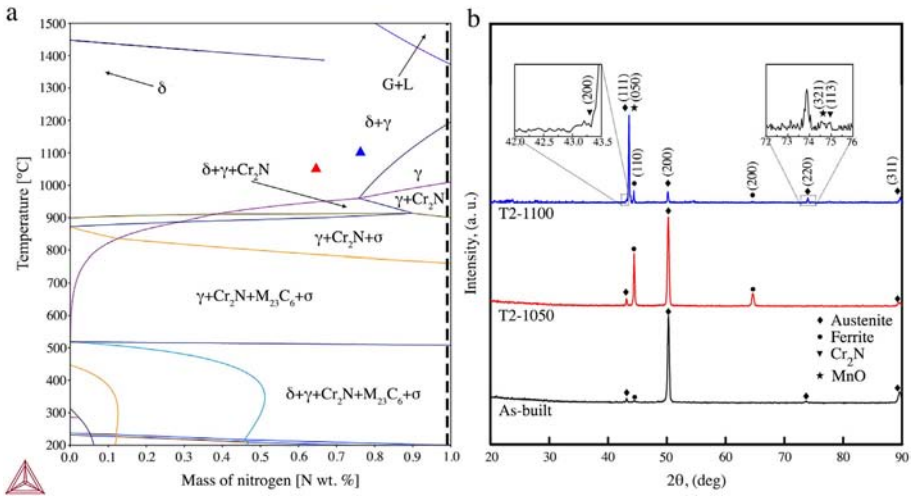

Fig. 9. (a) Equilibrium phase diagram of HNS0.99 calculated by Thermo-calc software and (b) the XRD images of the as-built, T2-1050 and T2-1100 samples.

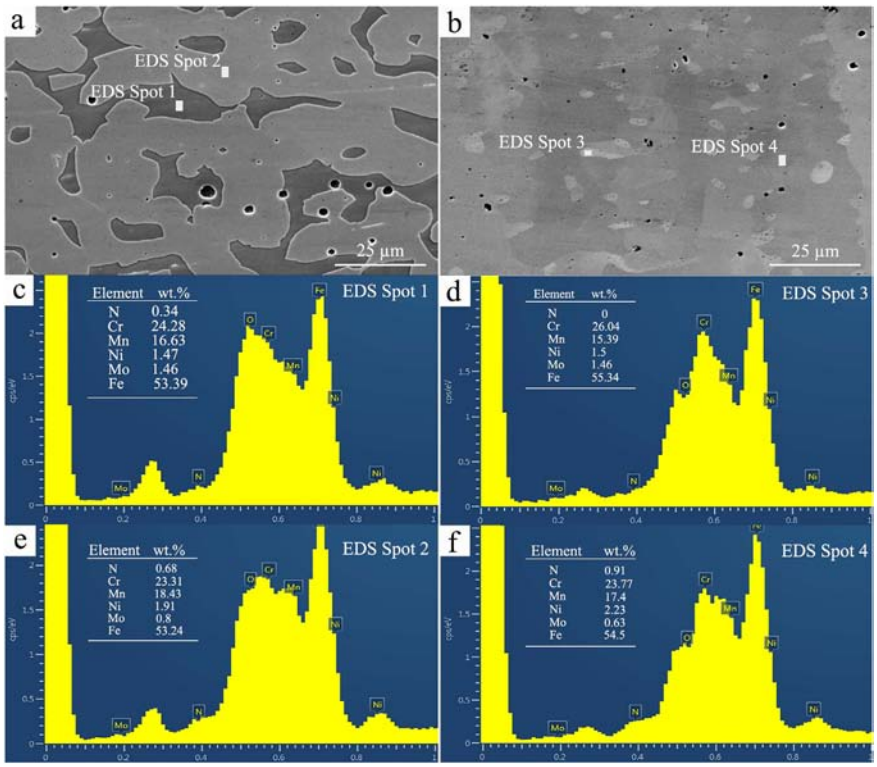

Fig. 10. SEM maps: (a) T2-1050 and (b) T2-1100 conditions, (c-f) EDS maps: corresponding to the EDS Spots 1 to 4, respectively.

(Fig. 16(a,b)). The lamellar step was around 30.6 μm which was in the range of the space between ferrite dendrites (around 33.6 μm) in the PLA, mentioned in chapter 3.1. The crack was confirmed propagation along the ferrite dendrites in the HD. Besides, inclusion islands also provided free sites for the crack, as shown in Fig. 16b. However, in VD, due to the high ductility of austenite matrix and the limited deformability of δ-ferrite dendrites and inclusion islands, they were extruded backwards during the necking process, as shown in Fig. 16(c,d). The lime green arrows represent the austenite flow direction, and the blue arrow shows the extrude backward direction of the δ-ferrite dendrite and the inclusion island. As a result, the fracture stress mainly concentrated in the austenite matrix, so, higher tensile ductility was well-reasoned.

However, no apparent evidence of the yield strength anisotropy in the HD and VD samples was found. This can be explained by the stable austenite made by the CMT-WAAM process and the nitrogen work hardening mechanism. Three VD specimens were selected from different conditions as the fracture mainly happened in the austenite matrix and their engineering curves along with true stress-strain curves were shown in Fig. 17. In these three conditions, no clear evidence of the transformation induced hardening behaviour was found. Due to the high content of Cr, Mn and nitrogen for this material, the temperature of

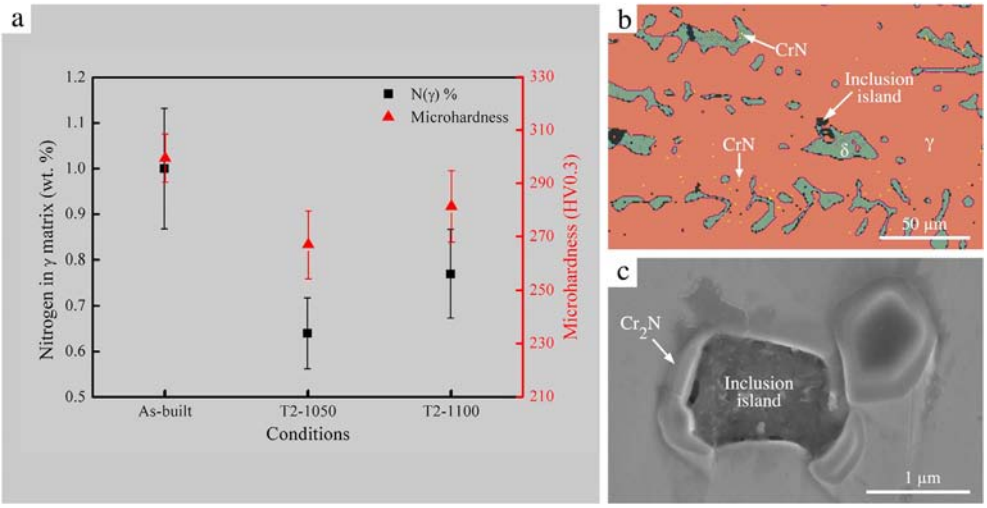

Fig. 11. (a) Changes of nitrogen concentrations in the γ matrix (N(γ)%) and microhardness of the as-built, T2-1050 and T2-1100 conditions (N(γ)% was measured by EDS detector and at least three points were taken for every sample), (b) EBSD phase diagram for the T2-1050 sample showing the austenite (ochre), ferrite (cyan), CrN (yellow) and inclusions (black), (c) rod-like Cr_2N precipitations around the inclusion island after condition T2-1100. (STEDVP was chosen for the calculation of error bars).

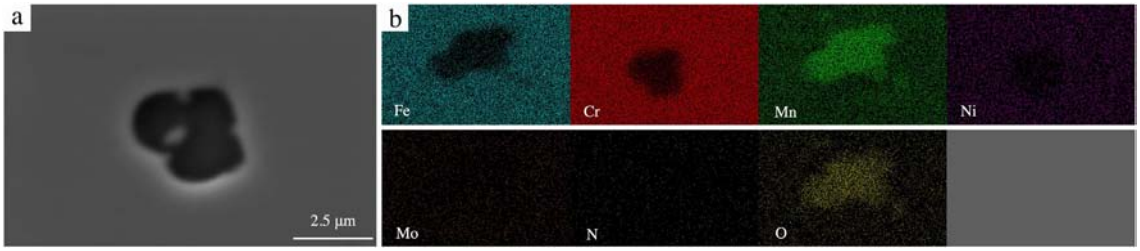

Fig. 12. (a) SEM image of inclusion island in the condition T2-1100 and (b) shows the EDS element concentration map.

martensite transformation was greatly under the room temperature according to Sjoberg [58] with the consideration of the independent effect of nitrogen:

$$M_{d30} = 608 - 515[\%C] - 821[\%N] - 7.8[\%Si] - 12[\%Mn] - 13[\%Cr] - 34[\%Ni] - 6.5[\%Mo]$$

As reported by Lee [59], the tension performance of these three conditions corresponded to the performance of the stable high nitrogen austenitic alloys. So, the austenite generated by deposition was stable.

The nitrogen work hardening effect was evident in Fig. 17b as the work hardening exponent kept constant even at high strains. Two T2-1050 tension samples (one was in HD and the other in VD) were selected to analysis the nitrogen work hardening effect. As the stable

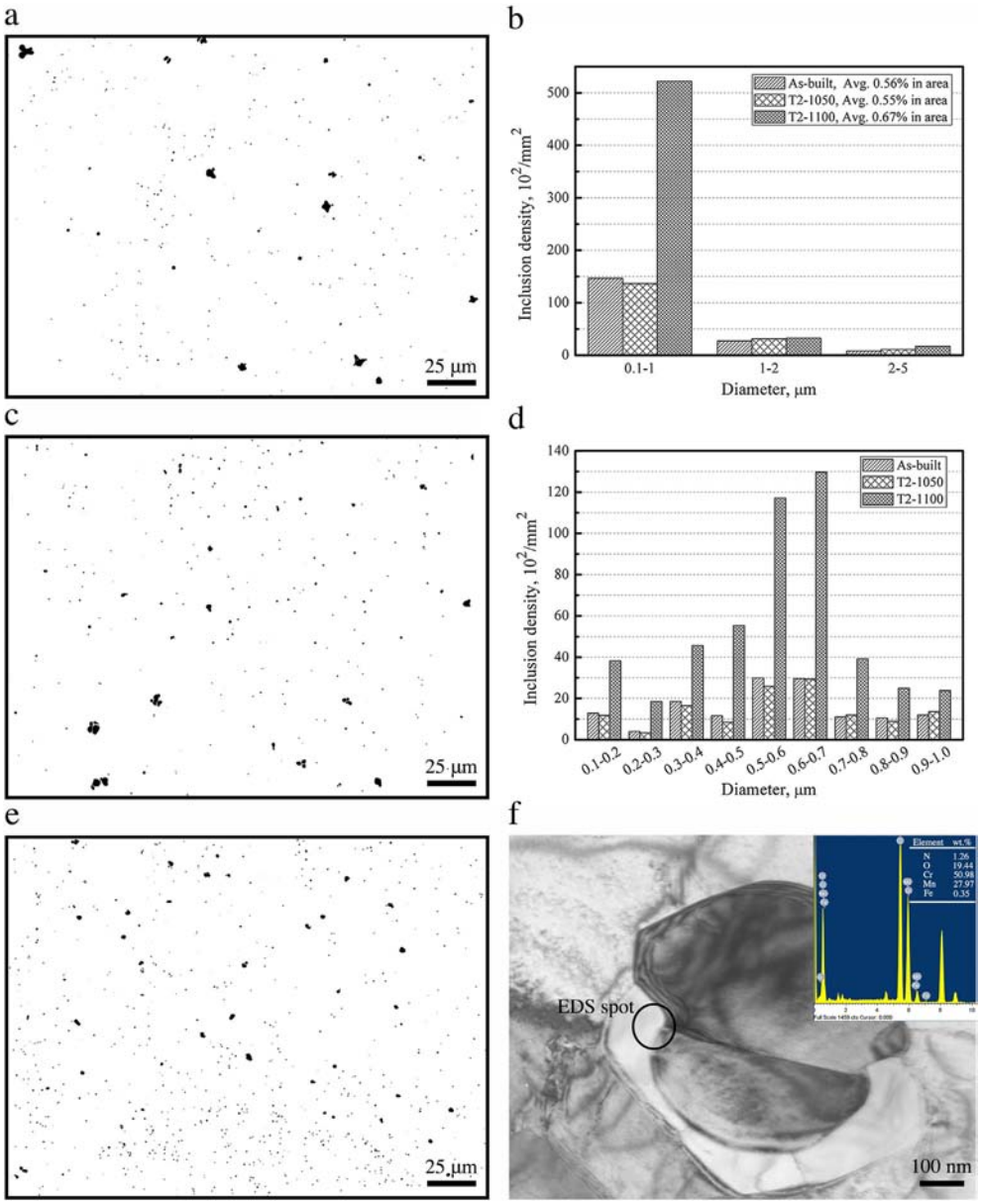

Fig. 13. OM images showing the distribution of inclusions: (a) as-built, (c) T2-1050 and (e) T2-1100 conditions, histograms of inclusion size and density distribution, for diameters from 0.1 to 5 μm showing in (b) and diameters from 0.1 to 1.0 μm showing in (d). (f): TEM image showing the MnO inclusion was surrounded by Cr_2N in T2-1100 condition and caused the enlargement of inclusions.

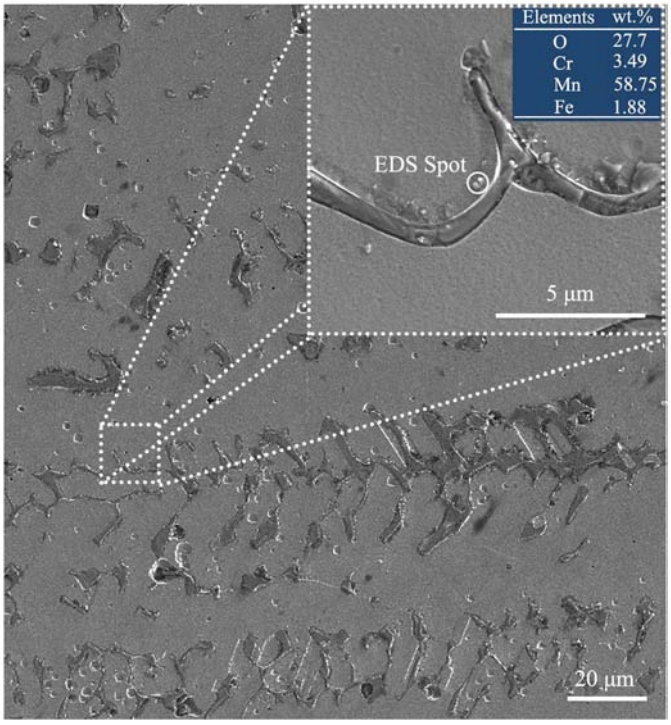

Fig. 14. SEM map of the as-built sample and the magnified inter-dendritic region, the element contents of the spherical inclusion was analyzed by EDS.

austenite made by the CMT-WAAM process, there was no transformation of martensite or twinning. According to Soussan [60], planar dislocation arrays would predominate the slip model in these high nitrogen stable austenite alloys. After checking by TEM, twinning or transformation induced martensite was not observed both in HD and VD samples as shown by Fig. 18a and b, respectively. Instead, some planes with dislocation-arrays seemed to overlap to make a kind of wall which sometimes looks like twinning. In Kubota's [61] report, the "twinning like" wall was called "dislocation-wall" which was formed by planar dislocations arrayed in different {111} planes. In Ren's study [62–64], deformation twins and high-density dislocation walls were the main forms of nitrogen work hardening effect due to the fine, entirely austenite grains combining with the applied stress. In this study, just dislocation-walls were found. Similarly, from [65,66], the planer dislocation array was commonly created during deformation of HNSs as nitrogen reduced the ability of cross-slip and limited the dislocations gliding in individual planes. As a result, during the early stage of deformation, parallel planer dislocation walls dominated the slip model in both HD and VD samples, which lead to the indistinctive YS.

However, at high strains, the work hardening exponent could be well maintained as the intersections of different dislocation walls, as shown in Fig. 18c. A set of new dislocations were generated at the intersection point of two slip planes, and they were called Lomer-Cottrell sessile dislocations [61]. This pinning effect was caused as the dislocations in different {111} plans would generate a new set of dislocations with the directions parallel to the [110] and lie in the {100} planes. Due to the {100} planes were not the slip planes for FCC metal, the sessile effect was well-reasoned. This pinning effect was very effective in preventing the motion of dislocations. The higher density of these sessile dislocations would be along with higher UTS and elongation values. From Fig. 18(a,b), plenty of sessile dislocations were revealed in both HD and VD directions, however, due to the side effect of ferrite dendrites and inclusion islands in the HD samples which made their UTS and elongation values lower than the VD samples (in Table 3).

In the next stage, the nitrogen content will be reduced in the wire to diminish the degassing process which caused the unstable arc and micropores in this study. Besides, lower heat input methods will be taken as the nitrogen content in the liquid phase was positive to the temperature of the molten pool. Oxygen will be moved from the shielding gas to reduce the oxide inclusion islands and make the nitrogen work hardening effect more positive.

5. Conclusion

In this study, the new high nitrogen Cr-Mn wire (HNS0.99) was used in the CMT-WAAM process, and two walls were made. One of them was cut and treated by high-temperature post heat treatment under different conditions. Microstructure evolution, inclusions and tension properties in different status were explored. The results of the study can be summarised as follows:

- High nitrogen austenite stainless steel parts were successfully made with excellent tension properties. The average N_γ wt% was1.0 for the as-built parts, 0.64 for the T2-1050 condition and 0.77 for the T2-1100 condition. The highest average values for the tension properties were 679.8 ± 12.9 MPa for YS, 931.6 ± 1.7 MPa for UTS and 39.5 ± 3.7% for elongation.
- Columnar austenite and δ-ferrite dendrites predominated the as-built microstructure. Two distinctive areas were explored in the matrix, ILA and PMA, and the former took the central part. FA solidification model was found in the ILA, and the AF model was revealed in the PMA. Nitrogen variation during solidification was the main reason for the erratic solidification behaviours.
- The inclusions were mainly composed of micropores and Mn oxides (supposed to be MnO) with uneven average area fractions in different conditions; 0.56% in the as-built, 0.55% in the T2-1050 and 0.67% in the T2-1100 conditions. The increased density of inclusions in 0.1–1 μm diameters was the main reason for the unpromising performance of tension properties of T2-1100 samples. The inducement for this increase is the formation of Cr_2N around the inclusions <0.1 μm in diameters.
- High-temperature short time heat treatment (T2-1050) demonstrated a great promotion of the YS and UTS due to the migration of δ-γ boundaries. However, in this study, high-temperature long time heat treatment (T2-1100) showed a detrimental effect to the tension properties owing to the enlarging of inclusions by Cr_2N.

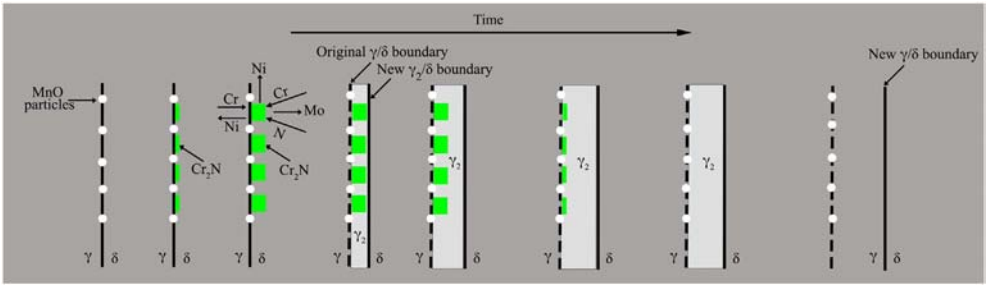

Fig. 15. Sketch of the growth mechanism of migration boundaries from the primary δ – MnO particles – γ to δ-γ_2 or δ-γ boundaries.

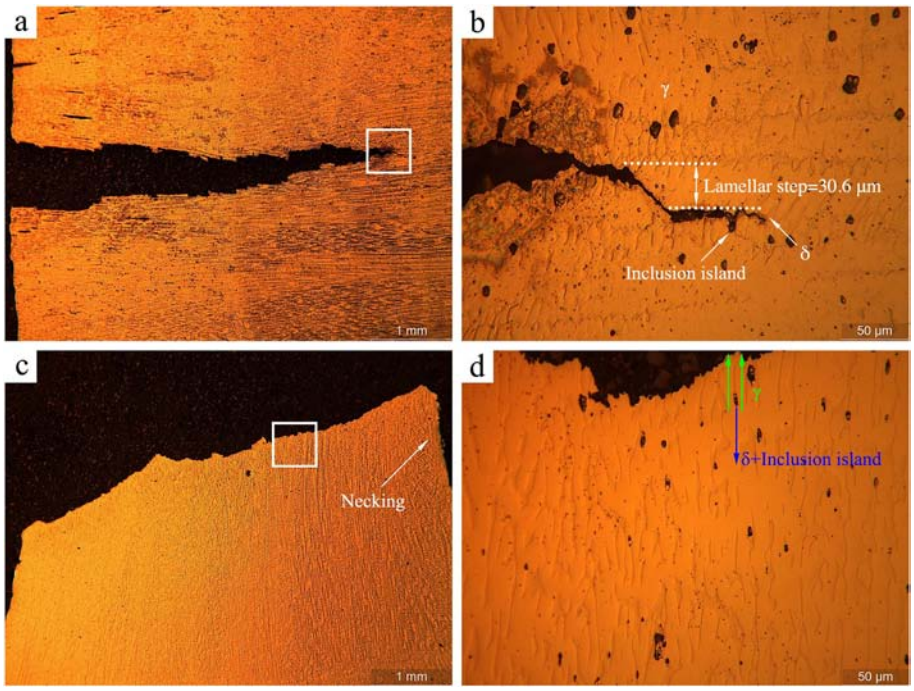

Fig. 16. (a) Cross section of the HD tension sample and (b) magnified zone of the white rectangle in 'a', showing the crack tip morphology, (c) cross section of the VD tension sample and (d) the magnified zone of white rectangle in 'c', showing the extruding texture during necking.

- YS and UTS anisotropies were largely reduced in this material due to the stable austenite matrix formed by the CMT-WAAM process and the nitrogen work hardening effect by the formation and intersection of planer dislocation walls both in VD and HD. However, the weakening effect of δ-ferrite dendrites which formed natural channels for the extension of cracks in the HD samples caused lower UTS and elongation values in this direction.
- In the future, lower nitrogen content in the wire, lower heat input and no oxygen in the shield gas will be carried out to reduce the ferrite number and inclusions in the WAAM made parts to maximise the positive effect of solid solution nitrogen.

Credit author statement

Dear editorial board of Materials and design:

This statement is to certify that all Authors have seen and approved the manuscript being submitted. And, the contributions of all authors are listed below.

Mr. Xiaoyong Zhang conceived the experiments, designed the analysis of microstructure and mechanical properties and wrote the paper.

Professor Qi Zhou and Kehong Wang provided the materials and equipment for this study, also made some comments on the mechanical property analysis and the grammatical analysis of this paper.

Dr. Yong Peng gave some suggestions on the experiment process such the selection of parameters and the anisotropy results analysis.

Dr. Jialuo Ding provided the analysis equipments such as EBSD and TEM, also gave some comments to the structure of this paper.

Professor Jian Kong gave some advices on the production of this high nitrogen Cr-Mn wire.

Professor Williams gave some suggestions on the logical frame of this paper and make some revisions for this paper. Based on their contributions, they are in the author list.

Acknowledgement

This research was supported by National Nature Science Foundation of China (No: 51505226). The authors wish to acknowledge the technician members of the Welding Engineering and Laser Processing Centre, Cranfield University and thank Dr. Xianwei Liu for the assistance during the SEM, EBSD and TEM analysis.

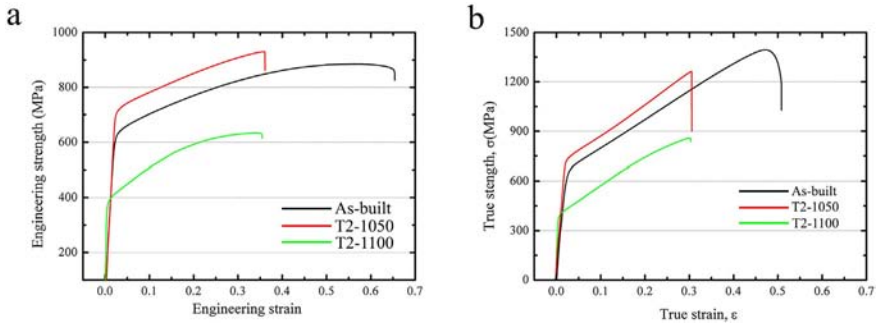

Fig. 17. (a) Engineering stress-strain curves and (b) true stress-strain curves the of as-built, T2-1050 and T2-1100 conditions.

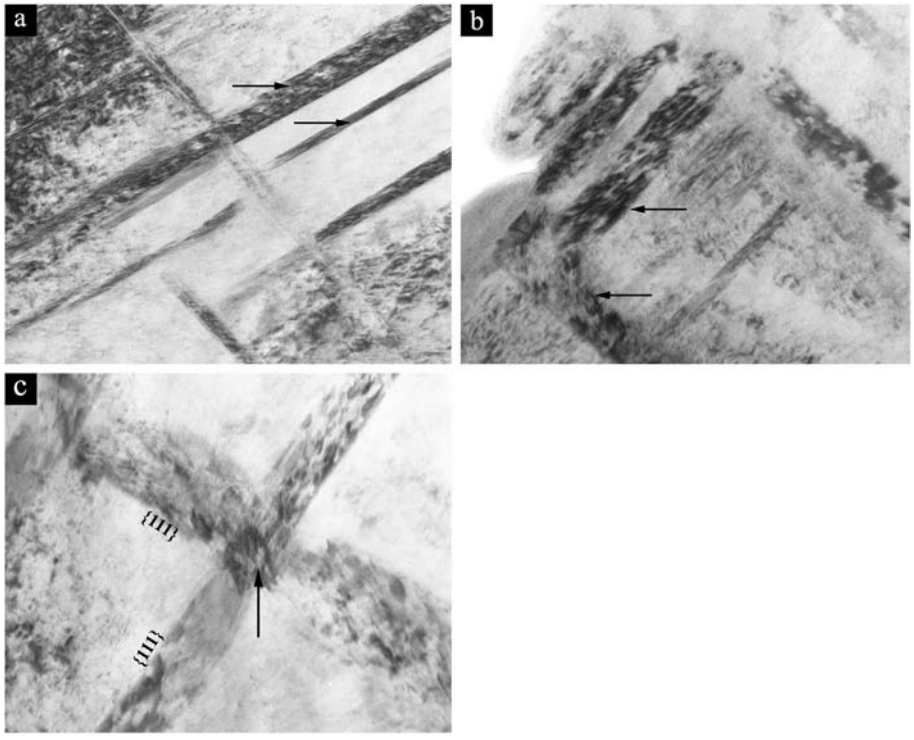

Fig. 18. Dislocation walls were generated in the fracture areas of the (a) HD and (b) VD T2-1050 samples, (c) the intersection point of two dislocation walls where clear sessile dislocations were observed.

Conflicts of interest

The authors declare no conflict of interest.

References

[1] M.O. Speidel, New nitrogen-bearing austenitic stainless steels with high strength and ductility, Met. Sci. Heat Treat. 47 (2005).
[2] V.G. Gavriljuk, Nitrogen in Iron and Steel, ISIJ Int. 36 (1996).
[3] Y.G. Lang, H.P. Qu, H.T. Chen, Y.Q. Weng, Research progres and development tendency of nitrogen-alloyed austenitic stainless steels, J. Iron Steel Res. Int. 22 (2015).
[4] F. Shi, P.C. Tian, N. Jia, Z.H. Ye, Y. Qi, C.M. Liu, X.W. Li, Improving intergranular corrosion resistance in a nickel-free and manganese-bearing high-nitrogen austenitic stainless steel through grain boundary character distribution optimization, Corros. Sci. 107 (2016) 49–59.
[5] Q.C. Wang, B.C. Zhang, Y.B. Ren, K. Yang, A self-healing stainless steel: role of nitrogen in eliminating detrimental effect of cold working on pitting corrosion resistance, Corros. Sci. 145 (2018) 55–66.
[6] H. Zhao, Y. Ren, J. Dong, K. Yang, The microstructure and tribological behavior of a pre-cold-deformed 0.90% nitrogen containing stainless steel, Mater. Werkst. 49 (2018) 1439–1448.
[7] G. Stein, I. Hucklenbroich, Manufacturing and Applications of High Nitrogen Steels, Conference Proceedings of the HNS, 2003 21–30 Switzerland.
[8] J.W. Simmons, W.E. Kemp, J.S. Dunning, The P/M processing of high-nitrogen stainless steels, JOM 48 (1996) 20–23.
[9] G. Balachandran, M.L. Bhatia, N.B. Ballal, P.K. Rao, Influence of thermal and mechanical processing on room temperature mechanical properties of nickel free high nitrogen austenitic stainless steels, ISIJ Int. 40 (2000).
[10] J.W. Simmons, Mechanical properties of isothermally aged high-nitrogen stainless steel, Metall. Mater. Trans. A. (1995) 26A.
[11] Z.H. Jiang, H.C. Zhu, H.B. Li, G.H. Liu, P.B. Wang, J.H. Zhu, S.C. Zhang, H. Feng, Effect of solidification pressure on interfacial heat transfer and solidification structure of 19Cr14Mn0.9N high nitrogen steel, ISIJ Int. 58 (2018) 107–113.
[12] L. Mosecker, Materials Design of High Nitrogen Manganese Austenitic Stainless TWIP Steels for Strip Casting, PhD Thesis RWTH Aachen University, 2016.
[13] S.W. Williams, F. Martina, A.C. Addison, J.L. Ding, G. Pardal, P. Colegrove, Wire + arc additive manufacturing, Mater. Sci. Technol. 32 (2016) 641–647.
[14] D.H. Ding, Z.X. Pan, D. Cuiuri, H.J. Li, Wire-feed additive manufacturing of metal components: technologies, developments and future interests, Int. J. Adv. Manuf. Technol. 81 (2015) 465–481.
[15] J. Bruckner, K. Himmelbauer, Cold Metal Transfer—Ein Neuer Prozess in der Fügetechnik, 2005.
[16] B.Q. Cong, J.L. Ding, S. Williams, Effect of arc mode in cold metal transfer process on porosity of additively manufactured Al-6.3%Cu alloy, Int. J. Adv. Manuf. Technol. 76 (2014) 1593–1606.
[17] J.L. Gu, J.L. Ding, S. Williams, H.M. Gu, P.H. Ma, Y.C. Zhai, The effect of inter-layer cold working and post-deposition heat treatment on porosity in additively manufactured aluminum alloys, J. Mater. Process. Technol. 230 (2016) 26–34.
[18] J.L. Gu, J.L. Ding, S. Williams, H.M. Gu, J. Bai, Y.C. Zhai, P.H. Ma, The strengthening effect of inter-layer cold working and post-deposition heat treatment on the additively manufactured Al–6.3Cu alloy, Mater. Sci. Eng. A 651 (2016) 18–26.
[19] J. Mehnen, J.L. Ding, H. Lockett, P. Kazanas, Design study for wire and arc additive manufacture, IJPD 19 (2014).
[20] X.F. Xu, S. Ganguly, J.L. Ding, S. Guo, S.W. Williams, F. Martina, Microstructural evolution and mechanical properties of maraging steel produced by wire + arc additive manufacture process, Mater. Charact. 143 (2017) 152–162.
[21] G. Posch, K. Chladil, H. Chladil, Material properties of CMT—metal additive manufactured duplex stainless steel blade-like geometries, Weld World. 61 (2017) 873–882.
[22] X.H. Chen, J. Li, X. Cheng, B. He, H. Wang, Z. Huang, Microstructure and mechanical properties of the austenitic stainless steel 316L fabricated by gas metal arc additive manufacturing, Mater. Sci. Eng. A 703 (2017) 567–577.
[23] Y.P. Lang, H.P. Qu, H.T. Chen, Y.Q. Weng, Research progress and development tendency of nitrogen-alloyed austenitic stainless steels, J. Iron Steel Res. Int. 22 (2015).
[24] M. Harzenmoser, Welding of high nitrogen steels, Mater. Manuf. Process. 19 (2004) 75–86.
[25] I. Woo, Y. Kikuchi, Weldability of high nitrogen stainless steel, ISIJ Int. 12 (2002).
[26] Y. Kikuchi, F. Matsuda, T. Okabe, M. Ohta, Nitrogen content of 316L weld metal and its fine particle by means of high-pressure MIG Arc welding, ISIJ Int. 36 (1996).
[27] T. Kuwana, H. Kokawa, S. Matsuzaki, Nitrogen absorption into weld metal under welding atmosphere of high pressure, Quart. J. Jpn. Weld. Soc. (1985) 3.
[28] L. Zhao, Z.L. Tian, Y. Peng, Porosity and nitrogen content of weld metal in laser welding of high nitrogen austenitic stainless steel, ISIJ Int. 47 (2007).
[29] W. Qiang, K.H. Wang, Shielding gas effects on double-sided synchronous autogenous GTA weldability of high nitrogen austenitic stainless steel, J. Mater. Process. Technol. 250 (2017) 169–181.
[30] M. du Toit, P.C. Pistorius, The influence of oxygen on the nitrogen content of autogenous stainless steel arc welds, Weld. J. 86 (2007) 222S–230S.
[31] M. du Toit, P.C. Pistorius, Nitrogen control during the autogenous arc welding of stainless steel - Part 2: a kinetic model for nitrogen absorption and desorption, Weld. J. 82 (2003) 231S–237S.
[32] V.G. Gavriljuk, H. Berns, High Nitrogen Steels: Structure, Properties, Manufacture, Applications, Springer, Berlin, 1999.
[33] H. Vashishtha, R.V. Taiwade, S. Sharma, A.P. Patil, Effect of welding processes on microstructural and mechanical properties of dissimilar weldments between conventional austenitic and high nitrogen austenitic stainless steels, J. Manuf. Process. 25 (2017) 49–59.
[34] R. Mohammed, G. Madhusudhan Reddy, K. Srinivasa Rao, Welding of nickel free high nitrogen stainless steel: microstructure and mechanical properties, Def. Technol. 13 (2017) 59–71.
[35] A. Poulalion, R. Botte, Nitrogen addition in steelmaking using nitriding ferroalloys, Processing of the 1st International Conference on High Nitrogen Steels HNS88, 1988.

[36] Y.C. Lin, P.Y. Chen, Effect of nitrogen content and retained ferrite on the residual stress in austenitic stainless steel weldments, Mater. Sci. Eng. A 307 (2001) 165–171.
[37] M.D. Tiot, P.C. Pistorius, Shielding gas oxygen additions as a means of curbing nitrogen degassing during the autogenous arc welding of nitrogen-alloyed stainless steel, Weld World. 53 (2009).
[38] J.W. Simmons, D.G. Atteridge, Microstructural characterization of as-cast high-nitrogen Fe-15Cr-15Ni alloys, J. Mater. Sci. 27 (1992).
[39] J.S. Liao, Nitride precipitation in weld HAZs of a duplex stainless steel, ISIJ Int. 41 (2001).
[40] A. Pramanik, A.K. Basak, Stainless Steel: Microstructure, Mechanical Properties and Methods of Application, Nova Science Pub Inc., USA, 2015.
[41] H. Feichtinger, G. Stein, Melting of high nitrogen steels, Mater. Sci. Forum 318-320 (1999) 261–270.
[42] C.S. Wu, Welding Thermal Processes and Weld Pool Behaviors, CRC Press, 2010.
[43] O. Hammar, U. Svensson, Solidification and Cast of Metals, The Metals Society, London, 1979.
[44] I. Moreno, J.F. Almagro, X. Llovet, Determination of nitrogen in duplex stainless steels by EPMA, Microchim. Acta 139 (2002).
[45] T.L. Zhang, Z.X. Li, S.D. Kou, H.Y. Jing, G.D. Li, H. Li, H. Jin Kim, Effect of inclusions on microstructure and toughness of deposited metals of self-shielded flux cored wires, Mater. Sci. Eng. A 628 (2015) 332–339.
[46] H.B. Li, Z.H. Jiang, H. Feng, Q.F. Ma, D.P. Zhan, Aging precipitation behavior of 18Cr-16Mn-2Mo-1. 1N high nitrogen austenitic stainless steel and its influences on mechanical properties, J. Iron Steel Res. Int. 19 (2012) 43–51.
[47] Z.R. Zhang, Z.Y. Zhao, C.Z. Li, Z.H. Jiang, H.B. Li, Role of aging precipitates on mechanical properties of HNS with different nitrogen content, Appl. Mech. Mater. 423–426 (2013).
[48] F. Vanderschaeve, R. Taillard, J. Foct, Discontinuous precipitation pf Cr2N in a high nitrogen, chromium-manganese austenitic stainless steel, J. Mater. Sci. 30 (1995).
[49] T.H. Lee, Time-temperature-precipitation characteristics of high-nitrogen austenitic Fe-18Cr-18Mn-2Mo-0.9N steel, Metall. Mater. Trans. A. 37 (2006) 3445–3454.
[50] I. Woo, M. Aritoshi, Y. Kikuchi, Metallurgical and mechanical properties of high nitrogen austenitic stainless steel friction welds, ISIJ Int. 42 (2002).
[51] H. Berns, V.G. Gavriljuk, S. Riedner, A. Tyshchenko, High strength stainless austenitic CrMnCN steels - part I: alloy design and properties, Steel Res. Int. 78 (2007) 714–719.
[52] H. Kokawa, E. Tsory, T.H. North, Nitride precipitation in duplex stainless steel weld metal, ISIJ Int. 35 (1995).
[53] D. Zhang, H. Terasaki, Y. Komizo, In situ observation of the formation of intragranular acicular ferrite at non-metallic inclusions in C–Mn steel, Acta Mater. 58 (2010) 1369–1378.
[54] S.S. Babu, The mechanism of acicular ferrite in weld deposits, Curr. Opin. Solid State Mater. Sci. 8 (2004) 267–278.
[55] M.D. Toit, P.C. Pistorius, The influence of oxygen on the nitrogen content of autogenous stainless steel arc welds, Weld. Res. (2007) 86.
[56] N. Kikuchi, S. Nabeshima, Y. Kishimoto, S. Sridhar, Micro-structure refinement in low carbon high manganese steels through Ti-deoxidation—inclusion precipitation and solidification structure, ISIJ Int. 48 (2008).
[57] O. Kamiya, Y. Kikuchi, H. Kobayashi, Mechanical characteristics of high nitrogen contained weld metal based on 316L stainless steel, Mater. Sci. Forum 318-320 (1999) 621–628.
[58] J. Sjoberg, Influence of analysis on the properties of stainless spring steel, Wire 23 (1973) 155–158.
[59] T.H. Lee, C.S. Oh, S.J. Kim, Effects of nitrogen on deformation-induced martensitic transformation in metastable austenitic Fe–18Cr–10Mn–N steels, Scr. Mater. 58 (2008) 110–113.
[60] A. Soussan, S. Degallaix, T. Magnin, Work-hardening behaviour of nitrogen-alloyed austenitic stainless steels, Mater. Sci. Eng. A (A142) (1991) 169–176.
[61] S. Kubota, Y. Xia, Y. Tomota, Work-hardening behavior and evolution of dislocation-micro-structures in high-nitrogen bearing austenitic steels, ISIJ Int. 38 (1998).
[62] F.Y. Dong, P. Zhang, J.C. Pang, Q.Q. Duan, Y.B. Ren, K. Yang, Z.F. Zhang, Microstructure and mechanical properties of high-nitrogen austenitic stainless steels subjected to equal-channel angular pressing, Acta Metall. Sin-Engl. 29 (2016) 140–149.
[63] H.C. Zhao, Y.B. Ren, J.H. Dong, X.M. Fan, K. Yang, Effect of cold deformation on the friction–Wear property of a biomedical nickel-free high-nitrogen stainless steel, Acta Metall. Sin-Engl. 29 (2016) 217–227.
[64] J. Li, Y.X. Yang, Y.B. Ren, J.H. Dong, K. Yang, Effect of cold deformation on corrosion fatigue behavior of nickel-free high nitrogen austenitic stainless steel for coronary stent application, J. Mater. Sci. Technol. 34 (2018) 660–665.
[65] S. Kubota, Y. Xia, Y. Tomota, Work-hardening behavior and evolution of dislocation-microstructures in high-nitrogen bearing austenitic steels, ISIJ Int. 38 (1998) 474–481.
[66] Y. Terazawa, T. Ando, T. Tsuchiyama, S. Takaki, Relationship between work hardening behaviour and deformation structure in Ni-free high nitrogen austenitic stainless steels, Steel Res. Int. (2009) 80.

https://dspace.org/

Study on microstructure and tensile properties of high nitrogen Cr-Mn steel processed by CMT wire and arc additive manufacturing

Zhang, Xiaoyong; Zhou, Qi; Wang, Kehong; Peng, Yong; Ding, Jialuo ...

2019-01-23
Elsevier
https://doi.org/10.1016/j.matdes.2019.107611
Zhang X, Zhou Q, Wang K, et al., (2019) Study on microstructure and tensile properties of high nitrogen Cr-Mn steel processed by CMT wire and arc additive manufacturing. Materials and Design, Volume 166, March 2019, Article number 107611

Downloaded from a DSpace repository. https://dspace.org/